

## AN ORIGINAL FLOW RULE FOR STRAIN-SPACE MULTI-SURFACE SAINT-VENANT PLASTICITY MODEL

Corado Ningre<sup>1</sup>, Guilhem Bles<sup>2</sup>, Ali Tourabi<sup>3</sup>, Didier Imbault<sup>4</sup>

<sup>1</sup> PhD Student, Univ. Grenoble Alpes, CNRS, Grenoble INP, 3SR, F-38000 Grenoble, France

<sup>2</sup> Associate Professor, ENSTA Bretagne, FRE CNRS 3744, IRDL, F-29200 Brest, France

<sup>3</sup> Associate Professor, Univ. Grenoble Alpes, CNRS, Grenoble INP, 3SR, F-38000 Grenoble, France

<sup>4</sup> Associate Professor, Univ. Grenoble Alpes, CNRS, Grenoble INP, 3SR, F-38000 Grenoble, France

### ABSTRACT

The one-dimensional Saint-Venant model can reproduce the elastic-plastic uniaxial behavior of metallic materials. A three-dimensional extension of this model is proposed, to simulate the cyclic elastic-plastic multiaxial behavior for complex loading paths. A multi-surface model is obtained and an original flow rule, defined in the strain space, is considered. This model has been implemented in a commercial finite element code. The model response is investigated for different loadings and compared to experimental data from the literature. The model showed accurate response in the multiaxial case of tension-torsion experiments.

### INTRODUCTION

The discrete generalized Saint-Venant model has been extended to the pure hysteresis continuous model by Persoz (1960), and has been studied in a more complete way by Guélin (1980). This model can reproduce the typical elastic-plastic behavior of metallic materials, in the case of a one-dimensional loading such as pure shear. The aim of this study is to propose an original flow rule, defined in the strain space (see Naghdi et al. (1975), Heiduschke (1995), Lee (1995) and Brown et al. (2003)), to extend the one-dimensional generalized Saint-Venant model to obtain a multiaxial elastic-plastic cyclic model. In the first part of this paper, the one-dimensional generalized Saint-Venant model is described. Then, an extension of this model to the three-dimensional case is presented. The last part of this work focuses on numerical results obtained after this model has been implemented in a commercial FEM code. These results are then compared to experimental data from the literature.

### ONE-DIMENSIONAL GENERALIZED SAINT-VENANT MODEL

In this section, a definition of the one-dimensional generalized Saint-Venant model is proposed, and its properties are illustrated. In the general three-dimensional case, the stress states and the plastic strains involved in an elastic-plastic behavior are deviatoric. Even if this section deals with the one-dimensional case, stress and strain scalars will be denoted  $\underline{\sigma}$  and  $\underline{\varepsilon}$  respectively, where the underlining recalls the deviatoric nature of stress and strain states, in anticipation for the three-dimensional extension.

#### *Definition and Illustration of the Resulting Behavior*

The one-dimensional elementary Saint-Venant model (or one-dimensional Saint-Venant element) is composed of a linear spring characterized by an elastic modulus  $G$  and a friction slider characterized by a threshold strain  $e$ , associated in series (Figure 1.a). If the strain of the element is less than its threshold value  $e$ , its behavior is that of the spring alone; the friction slider is locked. If the strain becomes greater than or equal to  $e$ , the friction slider unlocks and the spring strain remains fixed.

Figure 1.b illustrates the monotonic elastic-perfectly plastic behavior of this model. Saint-Venant parameters are defined by the pair  $(G, e)$ . The total strain  $\underline{\varepsilon}$  of the elementary model can be partitioned into an elastic strain  $\underline{\varepsilon}^e$  relative to the spring and a plastic strain  $\underline{\varepsilon}^p$  relative to the friction slider.

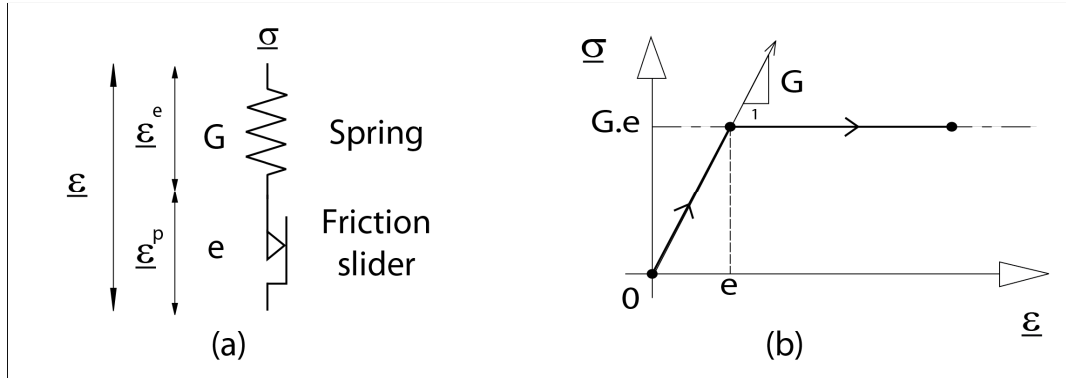


Figure 1. Elementary Saint-Venant model (a) and its mechanical response (b).

The one-dimensional two-element Saint-Venant model is composed of two elementary Saint-Venant models associated in parallel. It is characterized by the pairs  $(G_1, e_1)$ ,  $(G_2, e_2)$  such as  $e_1 < e_2$  (Figure 2.a). Its behavior results from the summation of the stresses  $\underline{\sigma}_1$  and  $\underline{\sigma}_2$ , applied on each element. The total strain is the same for the two elements due to the parallel construction. If the strain of the model is less than the first threshold  $e_1$ , the behavior is purely elastic and the two friction sliders are locked. If the strain becomes greater than or equal to  $e_1$ , the first friction slider unlocks and the first spring locks, hence a loss of rigidity of value  $G_1$  is recorded (Figure 2.b). Finally, if the strain of the model becomes greater than or equal to  $e_2$ , the behavior becomes perfectly plastic.

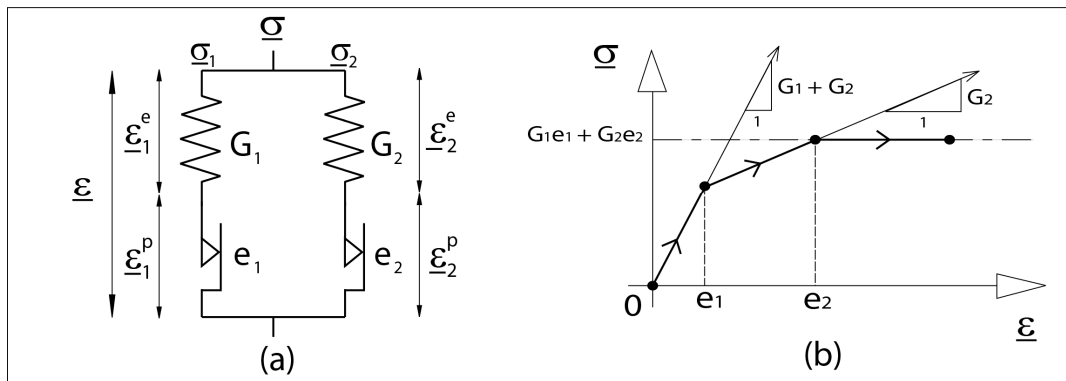


Figure 2. Two-element Saint-Venant model (a) and its mechanical response (b).

The one-dimensional generalized Saint-Venant model is characterized by a discrete sequence of  $n$  pairs  $(G_1, e_1), (G_2, e_2), \dots, (G_k, e_k), \dots, (G_n, e_n)$ . This sequence is distributed by ascending order of the thresholds strains:  $e_1 < e_2 < \dots < e_k < \dots < e_n$  (Figure 3.a). The first threshold  $e_1$  tends toward zero so that the behavior of the model is always irreversible. Nevertheless, a quasi-reversible behavior can be revealed by an infinitesimal loading close to the origin; it corresponds to an initial elastic modulus equal to the sum of all the spring elastic moduli  $G_k$ , i.e.  $\sum_{k=1}^n G_k$  (Figure 3.b). The total strain is the same for all the elements due to the parallel construction. As the strain increases, successive losses of rigidity are recorded, which correspond to the triggering of the thresholds strains  $e_k$ . For a large number  $n$  of elementary Saint-Venant models, the resulting behavior in the  $(\underline{\sigma}, \underline{\varepsilon})$  diagram tends towards a continuous behavior (Figure 3.b).

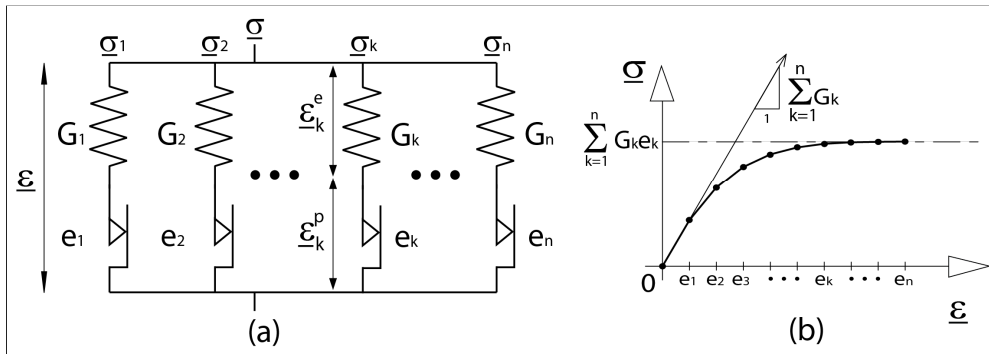


Figure 3. One-dimensional generalized Saint-Venant model (a) and its mechanical response (b).

**Intrinsic Properties**

The six essential intrinsic properties of the one-dimensional generalized Saint-Venant model are listed below (see Wack et al. (1992)):

1. The total strain in the model is the same for all the elements (Figure 3.a).
2. The first threshold strain tends toward zero, so that the model behavior is always irreversible (Figure 3.b).
3. At each reversal, all the friction sliders lock and the model gets back to its initial elastic modulus  $\sum_{k=1}^n G_k$  (Figure 4.a).
4. During a cyclic loading, the model observes Masing's rule. This is illustrated Figure 4.a, where the unload curve CD is the image of the first load curve OC, by a homothety of ratio -2 and center H. Thus, point N', on the CD curve, is the image of point N on the OC curve.
5. During complex cyclic loading, the model can memorize events such as load reversals. This is illustrated in Figure 4.a by the BAC reload and more particularly by the return to the first load behavior (OAC), after passing through point A.
6. Despite the irreversible behavior of the model, there is a neutral state that can be restored, after any mechanical loading, by a fundamental cycle. This property is illustrated by the cyclic loading OABACDE of Figure 4.a, which corresponds to an irreversible behavior, followed by a fundamental cycle EFO (Figure 4.b). This demagnetization-type cycle EFO consists of a cyclic loading of slowly decreasing strain amplitude through successive steps, until cancellation. The great property of a fundamental cycle is that a reload OG' after it shows a recovery of the initial behavior of first load (curve OG' is the same as curve OC, as illustrated on Figure 4.a).

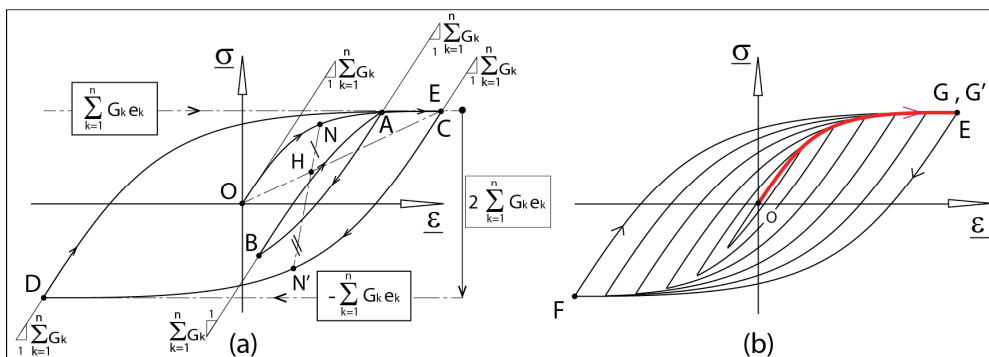


Figure 4. One-dimensional generalized Saint-Venant model behavior during a cyclic loading (a) and return to the neutral state by a fundamental cycle (b).

### Definition and Distribution of the Threshold Strains and Elastic Moduli

To define the model response, it is necessary to define the discrete sequence of the friction slider threshold strains  $e_k$  and the distribution of the spring elastic moduli  $G_k$ . To do so, two parameters ( $n, e_n$ ) are chosen, which are the total number of Saint-Venant elements and the threshold strain limit respectively. Then, the threshold strains are calculated as follows:

$$de = \frac{e_n}{n} \quad (1)$$

$$e_k = k \cdot de \quad \text{with } k \in [1, n] \quad (2)$$

To define the distribution of the spring elastic moduli  $G_k$ , a generative function  $s(\underline{\varepsilon})$  is adopted, such as:

$$s(\underline{\varepsilon}) = S_0 \cdot th\left(\frac{G_0}{S_0} \cdot \underline{\varepsilon}\right) \quad (3)$$

Where  $G_0$  represents the initial elastic modulus at the origin and  $S_0$  represents the yield limit. Figure 5 illustrates the shape of the generative function and its first and second derivatives, such as:

$$s'(\underline{\varepsilon}) = \frac{ds}{d\underline{\varepsilon}}(\underline{\varepsilon}) = G_0 \left\{ 1 - \left(\frac{s(\underline{\varepsilon})}{S_0}\right)^2 \right\} \quad (4)$$

$$s''(\underline{\varepsilon}) = \frac{d^2s}{d\underline{\varepsilon}^2}(\underline{\varepsilon}) = -2 \left(\frac{G_0}{S_0}\right)^2 s(\underline{\varepsilon}) \left\{ 1 - \left(\frac{s(\underline{\varepsilon})}{S_0}\right)^2 \right\} \quad (5)$$

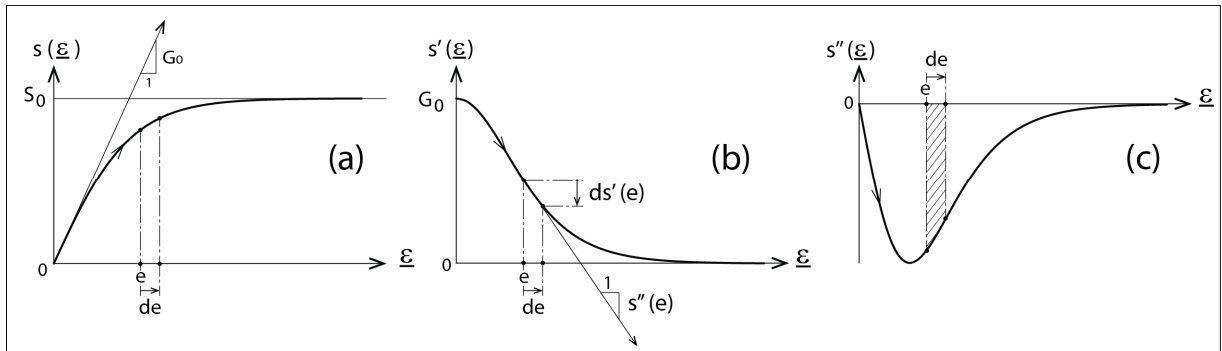


Figure 5. Generative function  $s(\underline{\varepsilon})$  (a), first derivative  $s'(\underline{\varepsilon})$  (b) and second derivative  $s''(\underline{\varepsilon})$  (c).

Let us consider the continuous one-dimensional generalized Saint-Venant model, which consists in replacing the discrete sequence of thresholds strains  $e_k$  by a continuous sequence of elements indexed by a continuous threshold  $e$ , varying from 0 to  $+\infty$ . In this case, a section between  $e$  and  $e + de$  is equivalent to an elementary Saint-Venant model with an elastic modulus  $-ds'(e)$  or  $-s''(e) \cdot de$ . Thus, for a discrete sequence of thresholds  $e_k$ , the spring elastic moduli  $G_k$  are distributed such as:

$$G_k = -s''(e_k) \cdot de \quad (6)$$

Where  $de$  is a constant defined by Equation 1. Figure 6 illustrates the shape of the distribution of the spring elastic moduli  $G_k$ .

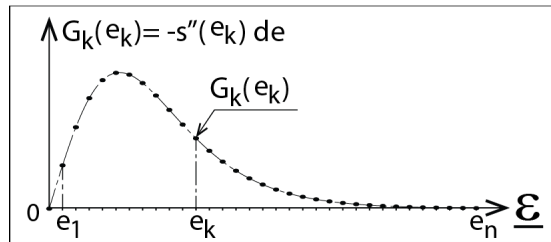


Figure 6. Distribution of spring elastic moduli  $G_k$ .

### One-Dimensional Generalized Saint-Venant Model with an Added Single Spring

The one-dimensional generalized Saint-Venant model can be completed with a single spring of elastic modulus  $G_\infty$  (Figure 7.a). This single spring then corresponds to an elementary Saint-Venant model characterized by an infinite threshold strain. In this case the quasi-reversible behavior, close to the origin and the load reversals, corresponds to an elastic modulus equal to the sum of all the spring elastic moduli, i.e.  $\sum_{k=1}^n G_k + G_\infty$  (Figure 7.b). The intersections between the straight line corresponding to the residual elastic modulus  $G_\infty$  and the y-axis, for  $\sigma > 0$  and  $\sigma < 0$ , are the limiting thresholds  $\pm \sum_{k=1}^n G_k e_k$  respectively, as illustrated on Figure 7.b.

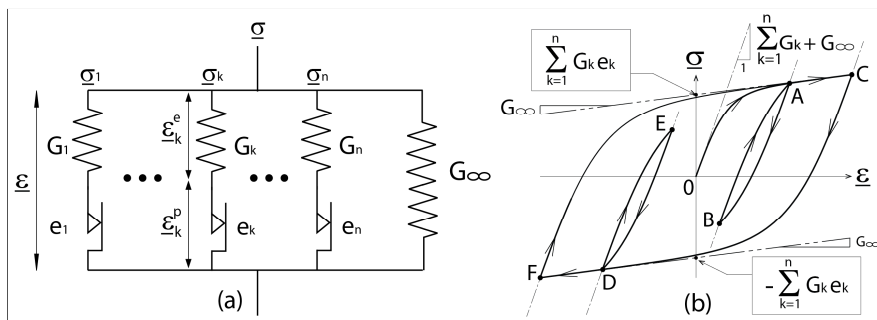


Figure 7. One-dimensional generalized Saint-Venant model completed with a single spring of elastic modulus  $G_\infty$  (a) and its mechanical response (b).

## THREE-DIMENSIONAL GENERALIZED SAINT-VENANT MODEL

In the three-dimensional case, the friction sliders of the one-dimensional generalized Saint-Venant model are represented by Von Mises-like yield surfaces. During the loading, it is necessary to consider the relative positions of these surfaces with respect to each other and the loading history. The yield surfaces are described in Ilyushin's five-dimensional deviatoric space (see Zyczkowski et al. (1984)), in which they are represented by hyperspheres. The deviatoric part of symmetric second order tensors are described by five components vectors in an orthonormal frame of Ilyushin's space (see Meggiolaro et al. (2016)).

In the remainder of this paragraph, the three-dimensional elementary Saint-Venant model and the three-dimensional generalized Saint-Venant are introduced. The yield surfaces and their movements are illustrated in the classical two-dimensional deviatoric plane.

### Three-Dimensional Elementary Saint-Venant Model

Figure 8 illustrates the extension of an elementary Saint-Venant model  $k$  from the one-dimensional case (Figure 8.a) to the three-dimensional case (Figure 8.b and Figure 8.c). We define the spring as an isotropic linear elastic behavior characterized by an elastic modulus  $G_k$  and we define the friction slider as a Von Mises-like yield surface, characterized by a threshold strain  $e_k$ .

During the loading, the yield surface remains fixed in the stress space and its radius remains constant, equal to the product  $G_k \cdot e_k$  (Figure 8.b). In the strain space, the radius of the yield surface remains constant during loading. The sliding of the friction slider, in the one-dimensional case, results in the plastic flow in the three-dimensional case. This flow corresponds to the evolution of the position of the yield surface center in the strain space. This position is parameterized by the plastic strain vector  $\vec{\varepsilon}_k^p$  (Figure 8.c). The elastic strain vector  $\vec{\varepsilon}_k^e$  can then be deduced from the total strain vector  $\vec{\varepsilon}$  by:

$$\vec{\varepsilon}_k^e = \vec{\varepsilon} - \vec{\varepsilon}_k^p \quad (7)$$

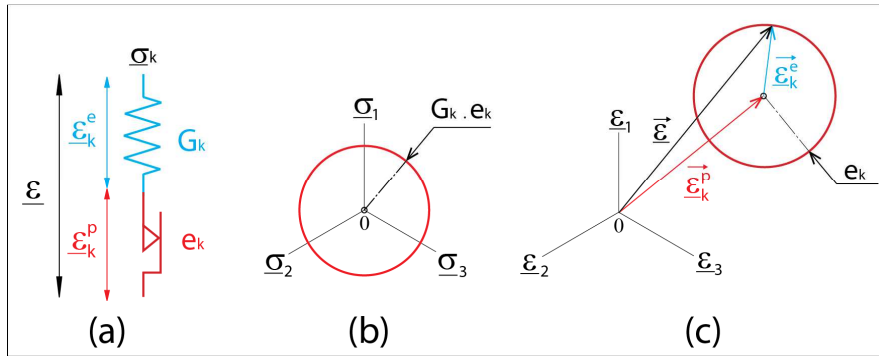


Figure 8. Elementary one-dimensional Saint-Venant model (a), three-dimensional stress-space (b) and strain-space (c) representations.

The movement of the yield surface in the strain space is driven by the flow rule. In this study, the normality flow rule, which implies that the plastic strain increment is orthogonal to the yield surface, is adopted. To define this motion, a vector  $\vec{V}_k$  is introduced, such as:

$$\vec{V}_k = \vec{\varepsilon}_k^e + d\vec{\varepsilon} \quad (8)$$

Where  $d\vec{\varepsilon}$  denotes a total strain increment during the loading, i.e. the transition from an instant  $t$  to an instant  $t + dt$  (Figure 9).

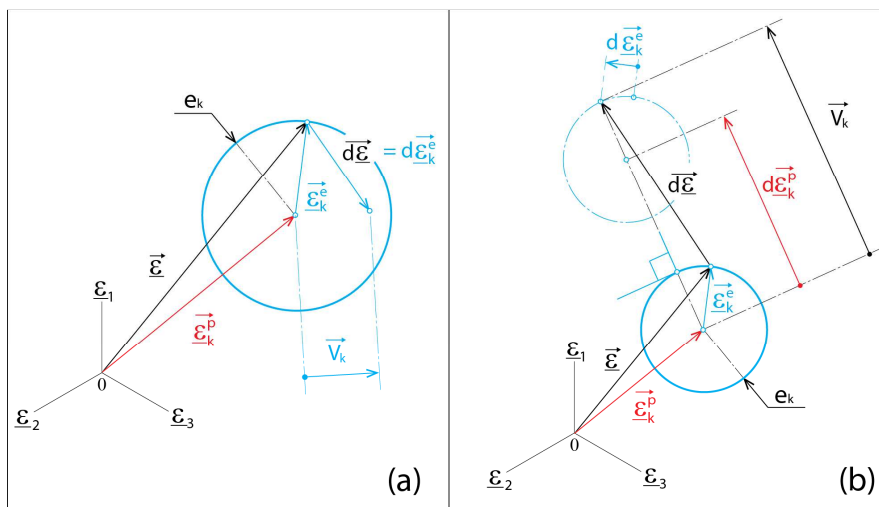


Figure 9. Illustration of the flow rule:  $\|\vec{V}_k\| \leq e_k$  (a),  $\|\vec{V}_k\| > e_k$  (b).

If the magnitude of vector  $\vec{V}_k$  is less than or equal to the radius of the yield surface, i.e.  $\|\vec{V}_k\| \leq e_k$ , the behavior is elastic and the center of the yield surface remains fixed (Figure 9.a):

$$\text{If } \|\vec{V}_k\| \leq e_k \text{ then } \overline{d\varepsilon_k^p} = \vec{0}; \overline{d\varepsilon_k^e} = \overline{d\varepsilon} \text{ and } \overline{d\sigma_k} = G_k \cdot \overline{d\varepsilon_k^e} \quad (9)$$

On the contrary, if the magnitude of vector  $\vec{V}_k$  is strictly greater than the radius of the yield surface, i.e.  $\|\vec{V}_k\| > e_k$ , then the behavior is elastic-plastic. In this case, the center of the yield surface moves along an increment of plastic strain  $\overline{d\varepsilon_k^p}$ , collinear to vector  $\vec{V}_k$ . This flow is then orthogonal to the yield surface and complies with the flow rule normality (Figure 9.b):

$$\text{If } \|\vec{V}_k\| > e_k \text{ then } \overline{d\varepsilon_k^p} = \left(1 - \frac{e_k}{\|\vec{V}_k\|}\right) \vec{V}_k; \overline{d\varepsilon_k^e} = \overline{d\varepsilon} - \overline{d\varepsilon_k^p} \text{ and } \overline{d\sigma_k} = G_k \cdot \overline{d\varepsilon_k^e} \quad (10)$$

### Three-Dimensional Generalized Saint-Venant Model

The three-dimensional generalized Saint-Venant model is characterized by a discrete sequence of threshold strains  $e_k$ , defined by Equation 2, and by a distribution of the elastic moduli  $G_k$ , defined by Equation 6. Figure 10 illustrates, in the two-dimensional deviatoric strain plane, the different yield surfaces corresponding to the discrete sequence of threshold strains. In the initial state, all the yield surfaces are centered at the origin of the deviatoric strain plane (Figure 10.a). During loading, all yield surfaces undergo the same total strain (Figure 10.b). The yield surfaces whose threshold has been reached slide (white yield surfaces on Figure 10.b) and the yield surfaces whose threshold has not been reached remain fixed (gray-colored yield surfaces, see Figure 10.b). In the two-dimensional deviatoric strain plane, a point such that E on Figure 10.a may be parameterized by a vector  $\vec{\varepsilon}$ , which depends on two parameters: radius  $Q_\varepsilon$  and phase  $\varphi_\varepsilon$ . Similarly, in the two-dimensional deviatoric stress plane, the pair  $(Q_\sigma, \varphi_\sigma)$  is the radius and the phase respectively of a stress vector  $\vec{\sigma}$ .

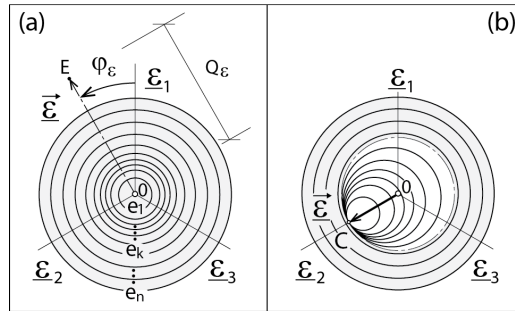


Figure 10. Illustration of yield surfaces in the two-dimensional deviatoric strain plane: initial state (a), state after a radial loading OC (b).

For each yield surface, the flow rule defined by Equation 9 and Equation 10 is adopted. That results in an independent movement of these surfaces, with respect to each other. This is illustrated in Figure 11, which shows simulation results in the two-dimensional deviatoric strain plane of three distinct loading paths that lead to the same point C: OC, OAbC, OABC (Figure 11.a). Figure 11.b shows the positions of the yield surfaces at the end of path OA. Figures 11.c and 11.d show the positions of the yield surfaces at points B and b respectively. Figures 10.b, 11.e and 11.f illustrate the final positions at point C of the yield surfaces, for each of the three loading paths. These three figures, which show relatively different configurations, illustrate a fundamental property of the model: it is highly sensitive to the loading history. This is confirmed by Figure 12.a, which gives distinct responses OC<sub>1</sub>, OAbC<sub>2</sub>, OABC<sub>3</sub>, in the deviatoric stress plane, for the three considered paths.

The rheological diagram ( $Q_\varepsilon, Q_\sigma$ ) (Figure 12.b) shows that the response of the two radial paths OA and OC<sub>1</sub> merge, even if their orientation is different in the deviatoric plane. Moreover, this figure clearly shows that points C<sub>1</sub>, C<sub>2</sub> and C<sub>3</sub> differ in stress while having the same total strain (see Figure 11.a). Also, Figure 12.c shows a phase difference effect between the strain in the deviatoric strain plane and the stress response in the deviatoric stress plane.

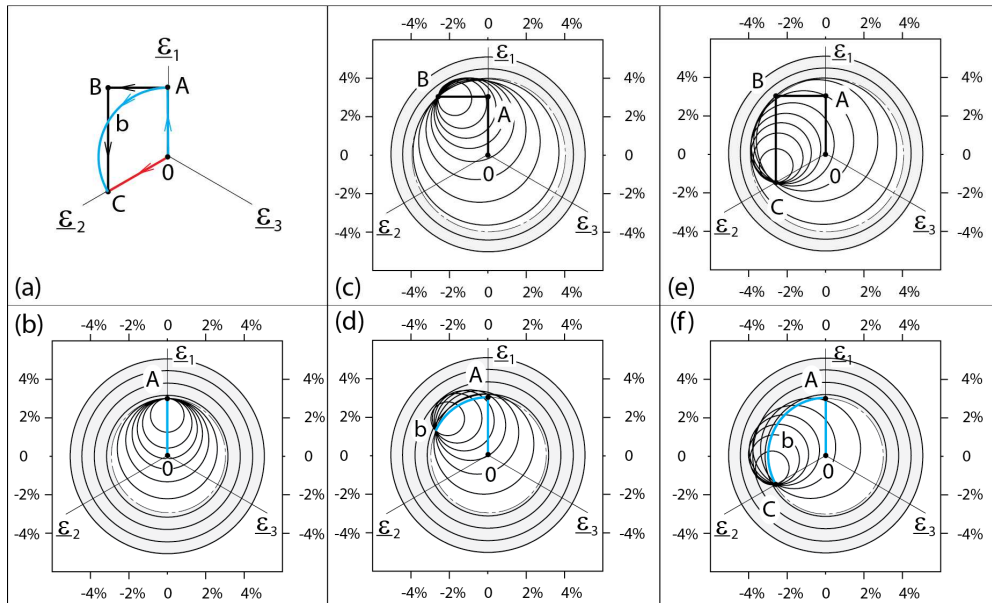


Figure 11. Simulations in the deviatoric strain plane of three loading paths: OC, OAbC, OABC (a); yield surfaces position at the end of: path OA (b), path OAB (c), OAb (d), OABC (e), OAbC (f). Model parameters:  $G_0 = 16 \text{ GPa}$ ,  $S_0 = 286 \text{ MPa}$ ,  $G_\infty = 1.6 \text{ GPa}$ ,  $n = 10$ ,  $e_n = 5 \%$ .

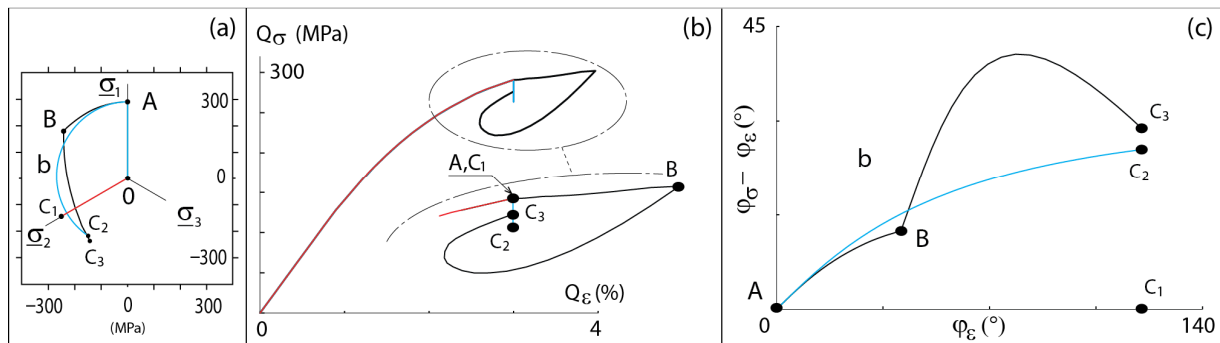


Figure 12. Simulation results related to Figure 11; stress responses OC<sub>1</sub>, OAbC<sub>2</sub>, OCBC<sub>3</sub>, in the deviatoric stress plane (a), corresponding to paths illustrated on Figure 11.a; responses in the rheological diagram ( $Q_\varepsilon, Q_\sigma$ ) (b); deviatoric-plane phase difference between stress and strain (c).

### Description of Cyclic Hardening Law Added to the Three-Dimensional Saint-Venant Model

To describe cyclic hardening or softening, the yield limit  $S_0$  is replaced by the yield limit  $S(\eta_1, \eta_2)$  (Figure 13), where  $\eta_1$  and  $\eta_2$  are two cyclic hardening variables. The variable  $\eta_1$  corresponds qualitatively to an indicator of cycle amplitude, while the variable  $\eta_2$  corresponds qualitatively to a cumulative indicator of the number of cycles. These two variables are calculated using an equivalent plastic strain of work hardening type, which considers the residual elastic modulus. The whole cyclic hardening law depends on three material parameters denoted by  $\gamma_2$ ,  $a_1$  and  $a_2$ .

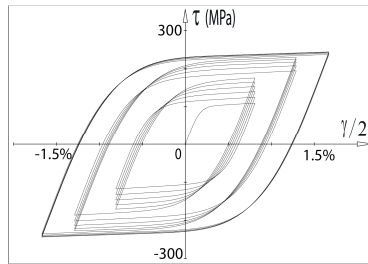


Figure 13. Illustration of the cyclic hardening law response in the case of a hardening material.

## IMPLEMENTATION IN FEM CODE AND SIMULATION RESULTS

### *Tensorial Formulation of the Model*

The constitutive equation is expressed with Cauchy stress tensor  $\boldsymbol{\sigma}$ , Almansi strain tensor  $\boldsymbol{\varepsilon}$  and Lamé coefficients  $(\lambda, \mu)$ . The model is written in Jaumann's co-rotational reference frame. This model can therefore take into account finite strains and finite rotations. The constitutive equation is in the form:

$$\boldsymbol{\sigma} = \left( \lambda + \frac{2\mu}{3} \right) \cdot \text{Tr}(\boldsymbol{\varepsilon}) \cdot \boldsymbol{\delta} + \sum_{k=1}^n G_k \cdot \underline{\boldsymbol{\varepsilon}}_k^e + G_\infty \cdot \boldsymbol{\varepsilon} \quad (11)$$

### *Implementation in FEM Code, Model Parameters and Identification*

The three-dimensional Saint-Venant model has been implemented in FEM code Abaqus (Abaqus 6.13 (2013)), using a user-subroutine UMAT. This subroutine contains 2 numerical parameters  $e_n$  and  $n$ , 4 material parameters for the pure hysteresis part  $G_0$ ,  $\nu$  (Poisson's ratio),  $S_0$  and  $G_\infty$ , and 3 material parameters for the cyclic hardening law  $\gamma_2$ ,  $a_1$  and  $a_2$ .

The four parameters of the pure hysteresis part are identifiable with a reduced number of uniaxial tensile tests (5 tests, for repeatability, are sufficient). The three cyclic hardening parameters can be identified with alternating torsion tests using the cyclic hardening and cyclic consolidation curves.

### *Validation of the Three-Dimensional Generalized Saint-Venant Model*

The three-dimensional generalized Saint-Venant model has been validated using confrontations with different experimental results. In this section, the pure hysteresis behavior without cyclic hardening is considered. An hourglass-type path in tension-torsion, performed by Aubin (2001) is considered (Figure 14.a). The four materials parameters have been identified with a monotonic uniaxial tensile curve. The simulation results, in bold lines Figure 14, reproduce in a very satisfactory manner the experimental data in dotted lines, either for the stress response (Figure 14.b), the response in the tensile direction (Figure 14.c) and the response in the shear direction (Figure 14.d).

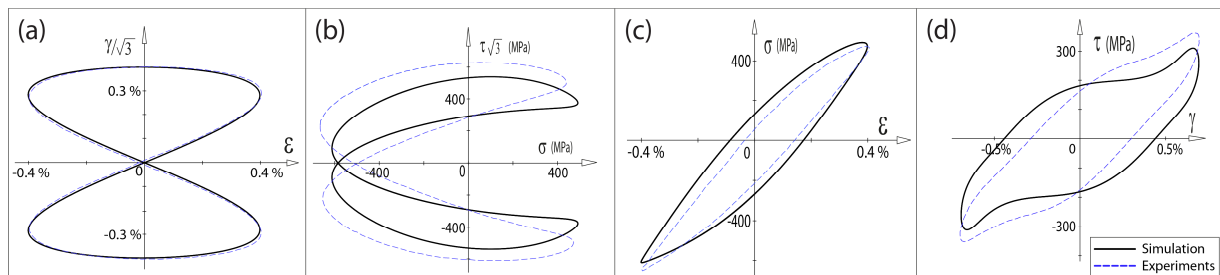


Figure 14. Simulated tension-torsion experiments (Aubin (2001)); strain path (a), stress (a), tensile (b) and shear (d) responses. Material parameters:  $G_0 = 145 \text{ GPa}$ ,  $\nu = 0.3$ ,  $S_0 = 530 \text{ MPa}$ ,  $G_\infty = 1410 \text{ MPa}$ .

## CONCLUSION

A three-dimensional extension of the generalized Saint-Venant model is proposed. The adopted normality flow rule allows multiaxial loading simulations in the strain space. This multiaxial elastic-plastic multi-surface model has a reduced number of parameters, easily identifiable by uniaxial tensile tests. A three-parameter cyclic hardening law is also proposed to capture the behavior evolution between the first load and the stabilized cycle. The model thus developed provides accurate results in the case of non-proportional loadings. Experimental tests are in progress and may complete this work, on the one hand to confirm the results obtained in pure hysteresis and on the other hand to validate the proposed cyclic hardening law.

## ACKNOWLEDGMENT

The support from GE Renewable Energies, Hydro'Like Chair and Fondation Grenoble INP is greatly appreciated.

## NOMENCLATURE

- $\mathbf{a}$  or  $\mathbf{A}$  : Symmetric second order tensor  
 $\underline{\mathbf{a}}$  or  $\underline{\mathbf{A}}$  : Deviatoric part of a symmetric second order tensor  
 $\vec{a}$  or  $\vec{A}$  : Vector (can be a symmetric second order tensor written in vector form)  
 $\underline{\vec{a}}$  or  $\underline{\vec{A}}$  : Deviatoric part of a second order tensor written in vector form  
 $a$  or  $A$  : Scalar  
 $\underline{a}$  or  $\underline{A}$  : Scalar where the underlining recalls its deviatoric nature  
 $\boldsymbol{\varepsilon}^e, \boldsymbol{\varepsilon}^p$  : Elastic part and plastic part of Almansi strain tensor respectively  
 $\boldsymbol{\delta}$  : Second order identity tensor

## REFERENCES

- Abaqus 6.13, (2013). "Abaqus documentation," *Dassault Systèmes Simulia Corp.*, Providence, RI, USA.
- Aubin, V., (2001). "Plasticité cyclique d'un acier inoxydable austéno-ferritique sous chargement biaxial non-proportionnel," *Ph.D. Thesis*, France.
- Brown, A.A., Casey, J., Nikkel, D.J., (2003). "Experiments conducted in the context of the strain-space formulation of plasticity," *Int. J. Plasticity*, 19 1965-2005.
- Guélin, P. (1980). "Remarques sur l'hystérésis mécanique," *J. Mécanique Théorique et Appliquée*, France, 19(2) 217-247.
- Heiduschke, K., (1995). "The logarithmic strain space description," *Int. J. Solids Structures*, 32 1047-1062.
- Lee, J.H., (1995). "Advantages of strain-space formulation in computational plasticity," *Computers and Structures*, 54 515-520.
- Meggiolaro, M.A., Pinho de Castro, J.T., Wu, H., (2016). "A general class of non-linear kinematic models to predict mean stress relaxation and multiaxial ratcheting in fatigue problems – Part I: Ilyushin spaces," *Int. J. Fatigue*, 82 158-166.
- Naghdi, P.M., Trapp, J.A., (1975). "The significance of formulating plasticity theory with reference to loading surfaces in strain space," *Int. J. Engng. Sci.*, 13 785-797.
- Persoz, B. (1960). "Introduction à l'étude de la rhéologie," *Dunod*, France.
- Wack, B., Tourabi, A., (1992). "Some remarks on macroscopic observations and related microscopic phenomena of the mechanical behavior of metallic materials," *Arch. Mech.*, 44 621-662.
- Zyczkowski, M., Kurtyka, T., (1984). "Generalized Ilyushin's spaces for a more adequate description of plastic hardening," *Acta Mechanica*, 52 1-13.